

Synthesis, Spectral, and X-ray Structural Characterization of Mixed Tetraamine-Barbitone Nickel (II) Complex Grafted g-C₃N₄ for Oxidative Stress and Cytotoxic Activities

Mohamed M. Ibrahim (✉ ibrahim@tu.edu.sa)

Taif University College of Science <https://orcid.org/0000-0002-4351-009X>

Gaber A. M. Meral

Taif University

Safaa N. Abdou

University of Taif

Mahmoud A. Mohamed

Cairo University

Mohamed Mohamed Soliman

Taif University

Salih Al-Juaid

King Abdulaziz University

Manal F. Abou Taleb

Prince Sattam Bin Abdulaziz University

Mohamed A. Amin

Taif University

Research Article

Keywords: Barbitone, Nickel(II) complex, g-C₃N₄, X-ray crystal Structures, Antioxidant/Cytotoxic Activities

Posted Date: January 19th, 2022

DOI: <https://doi.org/10.21203/rs.3.rs-1220104/v1>

License:  This work is licensed under a Creative Commons Attribution 4.0 International License.

[Read Full License](#)

Abstract

A new mixed ligand complex, viz., $[\text{Ni}(\text{Tren})(\text{Barb})(\text{H}_2\text{O})](\text{Barb})(\text{Barb-H})\cdot 2\text{H}_2\text{O}$ (NiC) {Tren = tris(2-aminoethyl)amine and Barb = 5,5-diethylbarbiturate} has been synthesized and characterized. The nickel(II) complex was grafted to $\text{g-C}_3\text{N}_4$, forming $\text{NiC@g-C}_3\text{N}_4$. The obtained NiC complex and its hybrid material $\text{NiC@g-C}_3\text{N}_4$ were characterized by means of FT-IR, TGA-DSC, UV-vis., SEM-EDX, and XRD. Single crystal X-ray crystallography suggests that NiC exhibits NiN_5O octahedral geometry. The results also show that the complex molecules are connected *via* $\text{N-H}\cdots\text{O}$ hydrogen bonds. The complex NiC and its $\text{NiC@g-C}_3\text{N}_4$ composite showed cytotoxic effects on *in vivo* experiments. They also showed an increase in tissue damage markers that are represented by the increase in tissue levels of malondialdehyde (MDA) in brain, liver, kidney and heart. In parallel, both materials showed inhibitory activity for examined antioxidants such as glutathione-S-transferase (GST), superoxide dismutase (SOD), glutathione (GSH), glutathione reductase (GSH-R). The destructive effects were clearer for the $\text{NiC@g-C}_3\text{N}_4$ composite compared to in liver, brain and kidney, respectively. The grafting of NiC complex in $\text{g-C}_3\text{N}_4$ is responsible for improving the catalytic activity, which is due to the synergistic effect of both components and facile recovery, as well recycling of the catalyst.

1. Introduction

Transition elements such as nickel acts as antioxidant agents to protect the body from oxygen-free radicals (O_2^-) that are formed during the oxidative stress process. This reduced form of the oxygen molecule leads to the oxidation of the main components of the cell, and thus leads to DNA damage if not resisted [1]. These radicals interact with each other to produce a more dangerous form. Where the superoxide anion (O_2^-) interacts with nitric oxide to produce both peroxide and nitrite [2, 3]. So it is therefore necessary that the solution lies in antioxidants or oxidative inhibitors that prevent the damage of these free radicals. As a result, professionals were able to solve the problem by administering large levels of superoxide dismutase (SOD) enzymes to the affected individuals. Unfortunately, due to the difficulties dealing with this protein due to its sensitivity and susceptibility to the surrounding environment, and thus its destruction, this technique did not function. Natural enzymes have huge molecular weights and hence cannot penetrate through the cell membrane, resulting in a local effect. As a result, the idea of synthesizing metal complexes that functionally mimic the active site of SOD has emerged and well developed [4–10].

The exploration of effective platforms for immobilizing of homogeneous metal complexes to develop hybrid catalysts is an attractive subject from the view of improving their catalytic activities with further advantages of facile recovery and reutilizing. Since nickel metal is easily accessible, non-toxic, and can be recognized as an ideal catalyst for many environmental and economical prospective.

The polymeric carbon nitride ($\text{g-C}_3\text{N}_4$) have been developed to be effective and environmentally nonthreatening catalysts. Immobilization of coordinated compounds on $\text{g-C}_3\text{N}_4$ [11–15] enhances its

photocatalytic activity. Moreover, its carbon structure with ordered nitrogen atoms arrangements not only improves its electronic and catalytic properties but also creates electrons and holes once visible light absorption [16–18].

As a part of our on-going research on the biological activities of several mononuclear nickel(II) and copper(II) complexes [4–10, 19] and as a continuation to the work on the synthesis and structures of metal complexes of the drug 5,5-diethylbarbiturate (Barb), which has sedative-hypnotic activity [7]. Herein, we synthesized a barbital-based Nickel (II) Complex (NiC), viz., $[\text{Ni}(\text{Tren})(\text{Barb})(\text{H}_2\text{O})](\text{Barb})(\text{Barb-H})\cdot 2\text{H}_2\text{O}$ (NiC) {TREN = tris(2-aminoethyl)amine and Barb = 5,5-diethylbarbiturate}. The prepared complex NiC was grafted to the $\text{g-C}_3\text{N}_4$ to obtain heterogenized catalyst ($\text{NiC}@g\text{-C}_3\text{N}_4$) (Scheme 1). Therefore, the current study in parallel aimed to examine whether these NiC and $\text{NiC}@g\text{-C}_3\text{N}_4$ synthesized compounds have the potential to act as scavengers and antioxidative stress for different organs such as brain, liver, kidney and heart after oral administration for 14 days.

2. Experimental

2.1 Materials and Instrumentations

The ligands tris(2-aminoethyl)amine (Tren) and Sodium 5,5-diethylbarbiturate (Barb) were purchased from Aldrich. The $\text{g-C}_3\text{N}_4$ was synthesized via a previously reported method [20]. Fourier transform infrared (FT-IR) spectroscopy were performed by means of a Bruker Alpha-Atunated FT-IR-spectrophotometer, in the range between 400 and 4000 cm^{-1} . Magnetic susceptibility was measured by using Gouy method at room temperature. UV-Vis. spectroscopy was performed using a Perkin Elmer Lambda 25 UV/Vis. XRD diffraction patterns were done using a D8 Advance (Bruker, USA) X-Ray diffractometer with $\text{Cu K}\alpha$ ($\lambda = 1.54056\text{ \AA}$) operated at 40 kV and 40 mA. The crystallographic data (Table 1) of the drug barbital (Barb-H) and its nickel(II) complex NiC were collected on a Smart CCD diffractometer of Bruker AXS using $\text{Mo-K}\alpha$ radiation. Lorentz-Polarization and absorption corrections were performed by SAINT and SADABS programs [21, 22]. The structures were solved by direct methods using SHELXL97 [23] and refined by full-matrix least-squares on F^2 with anisotropic displacement parameters for the non-H atoms using. Electron micrographs were taken for evaluation of the morphology with a scanning electron microscope (SEM) (Model JEOL JSM-6390LA).

2.1. Syntheses

2.1.1. Synthesis of nickel(II) complex $[\text{Ni}(\text{Tren})(\text{Barb})(\text{H}_2\text{O})](\text{Barb-H})_2\cdot 2\text{H}_2\text{O}$ NiC

The complex NiC prepared as follows was prepared as follows: By mixing a solution of 5,5-diethylbarbituric acid sodium salt (0.824 g, 4.0 mmol) in 10 mL of distilled water with 10 mL aqueous solution of $\text{Ni}(\text{NO}_3)_2\cdot 6\text{H}_2\text{O}$ (1.16 g, 4.0 mmol) The mixed solution was stirred for 30 min. Isopropanol (10

mL) was added to the cloudy solution. Tris(2-aminoethyl)amine (585 μ L, 4.0 mmol) was added drop-wise to the previous solution. The reaction mixture was stirred for further 1 hr at room temperature. After leaving the resulting solution aside for a week, purple-colored crystals of complex NiC were obtained. Anal. Calc. for $C_{30}H_{58}N_{10}NiO_{12}$ (809.57): Calcd. C, 44.51; H, 7.22; N, 17.30; Ni, 7.25. Found C, 44.39; H, 7.19; N, 17.42; Ni, 7.38.

Table 1
Crystal data and structure refinement of the drug Barb-H and its nickel(II) complex NiC.

	Barb-H	[Ni(Tren)(Barb)(H₂O)](Barb)(Barb-H)·2H₂O (NiC)
Empirical formula	C ₂₄ H ₃₆ N ₆ O ₉	C ₃₀ H ₅₈ N ₁₀ NiO ₁₂
Formula weight	552.59	809.57
Temperature [K]	100(2)	100(2)
Wavelength [Å]	0.71073	0.71073
Crystal system	trigonal	triclinic
Crystal colour	colorless	violet
Crystal size [mm]	0.080 x 0.220 x 0.400	0.150 x 0.250 x 0.450
Space group	R -3	P -1
Z	6	2
Volume [Å ³]	4174.8(5)	1893.9(3)
a [Å]	26.5928(14)	11.6159(10)
b [Å]	26.5928(14)	12.9821(11)
c [Å]	6.8167(4)	14.1121(12)
α[°]	90	98.074(2)
β[°]	90	91.503(2)
γ[°]	120	115.432(2)
Density(calc.) [g/cm ³]	1.319	1.420
Absorption coefficient [mm ⁻¹]	0.102	0.823
F(000)	1764	864
θ-range [°]	1.53 to 28.26	1.46 to 28.39
Index ranges	35<=h<=34	-15<=h<=15
	-34<=k<=35	-17<=k<=17
	-4<=l<=9	-18<=l<=17
Refinement method	Full-matrix least-squares on F ²	
Refinement program	SHELXL-2014 (Sheldrick, 2014)	

	Barb-H	[Ni(Tren)(Barb)(H ₂ O)](Barb)(Barb-H)·2H ₂ O (NiC)
Function minimized	$\Sigma w(F_o^2 - F_c^2)^2$	
Reflections collected	8524	33634
Independent reflections	2300 [R(int) = 0.0137]	9393 [R(int) = 0.0132]
Max. and min. transmission	0.9920 and 0.9600	0.9170 and 0.7790
Data /restraints / parameters	2300 / 0 / 120	9393 / 12 / 520
Goodness-of-fit on F ²	1.013	1.038
Final R indices	[2088 data; $l > 2\sigma(l)$], R1 = 0.0441, wR2 = 0.1323	8869 data; $l > 2\sigma(l)$, R1 = 0.0315, wR2 = 0.0881
R indices (all data)	R1 = 0.0340, wR2 = 0.0807	R1 = 0.0336, wR2 = 0.0901
Weighting scheme	$w = 1 / [\sigma^2(F_o^2) + (0.0401P)^2 + 4.6092P]$ where $P = (F_o^2 + 2F_c^2) / 3$	
Largest diff. peak [e.Å ⁻³] and hole	0.401 and -0.214	0.502 and -0.826
R.M.S. deviation from mean (eÅ ⁻³)	0.041	0.058

2.1.2. Synthesis of the heterogenized composite NiC@g-C₃N₄

To prepare 5% NiC@ g-C₃N₄ composite, 500 mg of g-C₃N₄ nanosheets were suspended in 50 ml of THF and under ultra-sound sonication for 1.0 h. Then 25 mg of nickel(II) complex NiC were added to the solution and further sonication for 1.0 h. The obtained NiC@ g-C₃N₄ composite were collected and dried at room temperature.

2.2. Animals

Male Albino rats weighting 200 ± 2.5 grams, 10 weeks age, were handled daily for a week to overcome injection and handling stress. Rats were maintained at 12 hours day light/dark cycle and at a temperature of 24 ± 2°C and humidity of 55 ± 5%. Animals gained complete free access to water and food.

2.2.1. Toxicity experiment.

The toxicity of newly synthesized compounds were evaluated in an experimental animal model by estimating the biochemical profiles including LD50 and activities of Glutamine pyruvate transferase enzyme (GPT) and lactate dehydrogenase (LDH). Seven rats per group were injected intraperitoneally

after overnight fasting with single dose of 100 mg kg⁻¹ body weight of synthesized compounds. The injections were continued for consecutive 14 days. Treatments were dissolved and suspended in DMSO. The toxicological effects were observed after 72 hrs of treatment in terms of mortality and expressed as LD50 [24]. Others determined after 14 days of administration according to methods of Reitman and Frankel [25] for GPT activity and Bergmeyer [26] for LDH activity.

2.2.2. Experimental design

After overnight fasting, rats were injected intraperitoneally with a single dose (100 mg/kg body weight) of the newly synthesized compounds, suspended in DMSO. Injection of synthesized compounds was maintained and continued for 14 consecutive days. Twenty-four hours after the last administration, rats were anaesthetized by isofluran inhalation then decapitated. The liver, brain, kidney and heart were taken under complete aseptic conditions, then washed and homogenized using Bio-rad tissue lyser in ice-cold physiological saline to prepare 10% (w/v) homogenate. The homogenate was centrifuged at 10000 rpm at 4°C for 10 minutes to remove cellular debris. The clear supernatant was taken for biochemical analysis.

2.2.3. The biochemical assays.

The glutathione-S-Transferase activity (GST) was estimated as described by Habig et al. [27]. Reaction mixture containing 50 mM phosphate buffer, pH 7.5, 1 mM of 1-chloro-2, 4 dinitrobenzene (CDNB) and an appropriate volume of compound solution. The reaction was initiated by the addition of reduced glutathione (GSH) and formation of S-(2, 4-dinitro phenyl) glutathione (DNP-GS). The activities were monitored as an increase in absorbance at 334 nm. The obtained values were expressed as μmol of CDNB conjugation formed per mg protein per minute. The superoxide dismutase (SOD) activity was measured through the inhibition of hydroxylamine oxidation by the superoxide radicals generated in the xanthine-xanthine oxidase system [28]. The results were expressed in units/mg protein. The reduced glutathione (GSH-R) levels in liver and kidney tissues were estimated based on methods of Ellman method [29], which measures the reduction of 5,5-dithio-bis (2-nitrobenzoic acid) (DTNB) (Ellman's reagent) by sulfhydryl groups to 2-nitro-5-mercaptobenzoic acid, which has an intense yellow color. The results were expressed in milligram per gram protein (mg/g protein). The tissue levels of malondialdehyde (MDA) in different tissues were measured based on method of Jain et al [30, 31] that based on thiobarbituric acid (TBA) reaction. The *Statistical analysis* of each measurement was determined in three replicate experiments, and the results were recorded as the means \pm standard deviation. Significant differences were indicated by $*p \leq 0.05$.

3. Results And Discussion

3.1. Characterization of mixed nickel(II) complex NiC and its functionalized hybrid material NiC@g-C₃N₄

In addition to the monodentate binding of the ligand barbital (Barb) to the nickel ion via imine nitrogen, the Barb unit acts as a balance in the composition of the formed nickel compound (NiC). The obtained NiC was immobilized to g-C₃N₄ nanosheets by taking the benefit of π - π interaction. The existence of nitrogen atoms on the sheets providing electron rich surface for the immobilization of NiC as shown in Scheme 1. The resulting nickel(II) compound and its functionalized hybrid material NiC@g-C₃N₄ were characterized using different methods of analysis such as elemental analysis, thermal analysis, magnetic susceptibility. In addition to FT-IR and electronic spectroscopies, X-ray diffraction provided evidences for their structures. The surface morphology of g-C₃N₄ nanosheet and its NiC@g-C₃N₄ composite has been explored with field emission scanning electron microscopy by using FE-SEM.

3.1. X-ray structures of Barb-H and its nickel(II) complex NiC

The molecular structures of ligand Barb-H and its nickel complex NiC have been determined by single crystal X-ray crystallography. Figure 1a illustrates the ORTEP drawing of the Barb ligand. The bond lengths and angles of the ligand (Table 2) are all in the range values of five free barbital anions [32], with the exception of the C-C ethyl bonds whose distances are little shorter (0.01 Å). The H-bonding network around barbital ions are illustrated in Figure 1b. The N-H group forms N-H...O(2) H-bonded dimers *via* a crystalline symmetry edge, such as those of calcium and barium barbital [33].

Table 2
Selected bond lengths (Å), bond angles (°), and hydrogen bond geometry of the drug Barb-H

Bond lengths [Å] and bond angles [°]:					
C1-C2	1.5216(11)	C2-C1-C4	114.22(7)	O2-C3-N2	121.98(8)
C1-C5	1.5454(12)	C4-C1-C5	109.20(7)	N2-C3-N1	116.34(7)
C2-O1	1.2138(11)	C4-C1-C7	106.96(7)	O3-C4-C1	121.48(7)
C3-O2	1.2172(10)	O1-C2-N1	120.16(8)	C6-C5-C1	114.11(7)
C3-N1	1.3777(10)	N1-C2-C1	117.83(7)	C2-C1-C5	108.90(7)
C4-N2	1.3695(11)	O2-C3-N1	121.67(8)	C2-C1-C7	108.18(7)
C1-C4	1.5235(11)	O3-C4-N2	119.91(8)	C5-C1-C7	109.28(7)
C1-C7	1.5556(12)	N2-C4-C1	118.55(7)	O1-C2-C1	122.01(8)
C2-N1	1.3806(11)				
C3-N2	1.3773(10)				
C4-O3	1.2188(10)				
C5-C6	1.5254(13)				

Hydrogen bond lengths [Å] and bond angles [°]:

D-H... A	D(D-H)	d(H... A)	d(D... A)	<(DHA)
N1-H1...O3	0.88	1.99	2.8571(9)	166.8
N2-H2...O2	0.88	2.00	2.8732(10)	169.0

Symmetry transformations used to generate equivalent atoms #1 $-x+1, -y, -z+1$ #2 $x+1/2, -y+1/2, z-1/2$

The nickel(II) complex (NiC) was crystallized in triclinic P-1 space group. The Ni(II) ion is coordinated by one Tren molecule, one N-bonded Barb ligand, and one water molecule in the form of a distorted octahedral environment: {water oxygen: Ni-O(1) = 2.1779(11) Å; Tren nitrogens: Ni-N(1) = 2.0959(10) Å, Ni-N(2) = 2.1009(12) Å, Ni-N(3) = 2.1116(12) Å, Ni-N(4) = 2.1254(11) Å; and Barb nitrogen: Ni-N(5) = 2.1366(11) Å} (Figure 2). These average bond distances and angles were well compared with those of other octahedral Ni (II) complexes, having N-donor atoms. [34–36]. The chelation is confirmed in complex NiC from the large deviation from 90° in its bond angles (Table 3). The structure also showed that the separate molecules are hydrated by two crystalized water molecules as well as uncoordinated basic and acidic Barb-H molecules [37]. These solvated acidic Barb-H by water molecules are involved in a number of strong H-bonds {N-H...O and O-H...O} (Figure 3) in nickel(II) complex NiC and forms 1D-supramolecular chains running the *c* axis.

Table 3

Selected bond lengths (Å), bond angles (°), and hydrogen bond geometry of nickel(II) complex NiC.

Bond lengths [Å] and bond angles [°]:					
Ni(1)-N(1)	2.0959(10)	N3-Ni1-O1	83.35(5)	Ni1-N2-H1	112.5(18)
Ni(1)-N(2)	2.1009(12)	N1-Ni1-N3	160.91(5)	Ni1-N2-H2	111.4(19)
Ni(1)-N(3)	2.1116(12)	N1-Ni1-N4	82.90(4)	C2-N3-Ni1	111.84(9)
Ni(1)-N(4)	2.1254(11)	N3-Ni1-N4	81.62(5)	Ni1-N3-H3A	109.2
Ni(1)-N(5)	2.1366(11)	N2-Ni1-N5	93.15(5)	Ni1-N3-H3B	109.2
Ni(1)-O(1)	2.1779(11)	N4-Ni1-N5	175.12(4)	C5-N4-Ni1	109.62(8)
C21-O8	1.2421(16)	N1-Ni1-N2	92.27(5)	N2-Ni1-O1	174.20(6)
C25-O6	1.2123(16)	N2-Ni1-N3	96.64(5)	N4-Ni1-O1	92.04(5)
C26-O5	1.2139(16)	N2-Ni1-N4	82.23(5)	C3-N1-Ni1	110.83(8)
C27-O7	1.2216(15)	N1-Ni1-N5	98.91(4)	Ni1-N1-H1A	109.5
C30-O11	1.2412(15)	N3-Ni1-N5	97.43(5)	Ni1-N1-H1B	109.5
C31-O12	1.2209(15)	N1-Ni1-O1	86.11(4)	C6-N2-Ni1	108.16(9)
N1-Ni1-O1	86.11(4)	C6-N2-Ni1	108.16(9)		

Hydrogen bond lengths [Å] and bond angles [°]:

D-H... A	D(D-H)	d(H... A)	d(D... A)	<(DHA)
N2-H1...O10	0.877(10)	2.496(18)	3.234(2)	142.0
N2-H2...O5	0.864(10)	2.123(13)	2.9389(16)	157.0
N1-H1A...O2	0.99	2.32	2.9694(15)	122.5
N1-H1B...O8	0.99	1.98	2.9218(14)	158.1
N3-H3A...O1	0.99	2.4	3.3353(17)	156.7
N3-H3A...O4	0.99	2.39	2.9359(16)	114.4
N3-H3B...O11	0.99	2.26	3.0227(15)	132.6
N9-H40...O11	0.88	1.92	2.7797(14)	166.0
N11-H11A...O7	0.88	2.09	2.9611(14)	168.9
O10-H11W...O3	0.883(10)	1.947(10)	2.821(2)	170.0
O10-H12W...O3	0.889(10)	2.184(12)	3.051(2)	165.0
O9-H9W...O8	0.839(9)	1.909(10)	2.7459(14)	175.0
O9-H10W...O2	0.827(9)	2.242(12)	3.0451(15)	164.0
N6-H50...O2	0.72(2)	2.12(2)	2.8112(19)	162.0
N8-H51...O9	0.79(2)	2.03(2)	2.8195(14)	177.0
O1-H1W...N12	0.834(9)	1.930(10)	2.7604(15)	174.0
O1-H2W...O4	0.827(10)	2.262(16)	3.0422(17)	157.0

Symmetry transformations used to generate equivalent atoms: #1 -x+2,-y,-z+2 #2 -x+1,-y,-z+2

Figure 4 illustrates the infrared spectra of NiC, and g-C₃N₄ nanosheets, as well as the hybrid composite NiC@g-C₃N₄. The IR spectrum of NiC displays several sharp bands in the middle of the IR region, evidently confirming the existence of the barbital unit [33]. The detected ν_{NH} stretching vibration band at 3180 cm⁻¹ for the ligand was shifted to the higher energy 3198 cm⁻¹, confirming the formation of hydrogen bonds. Symmetric and asymmetric absorption bands appeared in the range of 3245–3325 cm⁻¹, indicating the presence of NH₂ groups of the TREN ligand. Sharp absorption bands were observed in the frequency range 1609–1715 cm⁻¹, assigning the $\nu(\text{C}=\text{O})$ of the barbital ligand, indicating the non-coordination of the barbital ligand to the nickel ions *via* the C=O oxygen donors.

The IR spectrum of g-C₃N₄ nanosheets displays a sharp absorption band at 815 cm⁻¹, characteristic to the triazine units. The spectrum also shows absorption band at 1637 cm⁻¹, attributing to the stretching $\nu(\text{C}=\text{N})$ absorption mode, while the bands at 1240, 1315, and 1413 cm⁻¹ are assigned to the aromatic stretching $\nu(\text{C}-\text{N})$ vibration mode. Also broad vibration band between of 3000 and 3450 cm⁻¹, indicating to

the stretching mode of $-\text{NH}_2$ or to the vibrations of N-H group in $\text{g-C}_3\text{N}_4$ nanosheets. Upon immobilization of nickel(II) complex NiC to $\text{g-C}_3\text{N}_4$ nanosheets, the IR spectrum of the hybrid composite $\text{NiC@g-C}_3\text{N}_4$ shows new three absorption bands at 1639, 1417 and 1245 cm^{-1} , confirming the existence of NiC complex units in the produced composite.

Investigation of the UV-vis. electronic spectroscopies of NiC, $\text{g-C}_3\text{N}_4$ nanosheets, and $\text{NiC@g-C}_3\text{N}_4$ were shown in figure 5. The nickel(II) complex NiC reveals an extreme band at λ_{max} 286 nm, indicating the inter-ligand $\pi \rightarrow \pi^*$ transition in barbitol ligand. Whereas, a less intense band at 553 nm is attributing to the nickel $d(\pi) \rightarrow \pi^*$ MLCT transition [38].

The electronic spectrum of $\text{g-C}_3\text{N}_4$ nanosheets exhibits an absorption band similar to that found in the absorption spectrum of semiconductor between 200-450 nm. This may be owing to the charge transference from the valence band of nitrogen atom (2p orbitals) to the conduction band of carbon atom (2p orbitals) in the $\text{g-C}_3\text{N}_4$. Also a sharp band was observed at 244 nm, attributing to the aromatic transition ($\pi \rightarrow \pi^*$). While another band around 377 nm was characterizing to the nitrogen nonbonding ($n \rightarrow \pi^*$) transition. Comparing to $\text{g-C}_3\text{N}_4$ nanosheets, the produced composite $\text{NiC@g-C}_3\text{N}_4$ shows a sharp peak at 533 nm due to the presence of nickel(II) complex MLCT transition, which confirms the successful attachment of the nickel(II) complex NiC to carbon nitride [39]. The magnetic moment of NiC complex was measured to be 2.87 B.M, confirming its paramagnetism and octahedral configuration. Where this value is normally observed for octahedral nickel(II) complexes (2.5-3.5 B.M.) [7] with two unpaired electrons.

The thermogravimetric-differential scanning calorimetry (TGA-DSC) thermogram of NiC complex showed that the decomposition takes place in several stages (Figure 6). It exhibits weight loss of 3.17% (Calc. 3.25%) with an exothermic, assignable to the removal of one coordinated water molecule. This process is followed by a strong endothermic peak at $285.0\text{ }^\circ\text{C}$, which has a total weight loss of 63.51% (Calc. 64.11%). This may be attributed to the loss of 1.7 barbitol moieties, forming a mixture of $2\text{NiO} + \text{C}$ as a final solid product (Found 18.45%; Calc. 19.08%).

The thermal stability of $\text{g-C}_3\text{N}_4$ nanosheets and $\text{NiC@g-C}_3\text{N}_4$ is also determined (figure 5a). The TGA-DSC thermogram of $\text{g-C}_3\text{N}_4$ nanosheets displays a weight loss between 540 to $730\text{ }^\circ\text{C}$, which can be ascribed to the decomposition of $\text{g-C}_3\text{N}_4$ (**figure 6b**) [40, 41]. Similar thermal behavior is also observed in the same range is for $\text{NiC@g-C}_3\text{N}_4$ (figure 6c). Besides, the $\text{NiC@g-C}_3\text{N}_4$ thermogram reveals a mass loss in the range of $210\text{-}300\text{ }^\circ\text{C}$, which can be owing to the loss of barbitol units of nickel(II) complex NiC from the surface of $\text{g-C}_3\text{N}_4$.

The surface morphology of $\text{g-C}_3\text{N}_4$ and $\text{NiC@g-C}_3\text{N}_4$ has been explored by using SEM images with EDX and Mapping (figure 7). The obtained $\text{g-C}_3\text{N}_4$ nanosheet showed thin crumpled and coated graphene-like sheets. The $\text{g-C}_3\text{N}_4$ framework has a parallel π -conjugated system of substituted nitrogen atoms as in the graphitic planes, which are made due to sp^2 hybridization between carbon and nitrogen atoms (figure

7a). For the case of NiC@g-C₃N₄ (figure 7b), the crumpled nature of g-C₃N₄ nanosheets was increased and expanded due to the non-covalent π - π interaction between NiC and the surface. The EDX pattern of NiC@g-C₃N₄ shows the presence of nickel(II) ions in the constructed composite (figures 7c and 7d). Also the SEM elemental mapping shows homogeneous spreading of nickel complex moieties on the surface of g-C₃N₄ in the obtained composite (figures 7e and 7f).

The XRD pattern of g-C₃N₄ nanosheet demonstrates a distinguishing peak at 27.4°, that can be indexed as the (002) diffraction plane having 0.32 nm interlayer distance. This is mostly owing to the accumulation of graphite like conjugated triazine aromatic sheets and matches well with JCPDS 87–1526 for npg-C₃N₄ [42]. Further observation, for the g-C₃N₄ nanosheet, the intensity of diffraction peak for the (100) crystal planes almost disappeared [42]. Immobilization of nickel(II) complex NiC on g-C₃N₄ nanosheet has no effect on the phase construction of the carbon nitride; however the strength of the peak has a little increase. This is mainly due to the stacking of the nickel(II) complex on the carbon nitride support (figure 8).

3.2. Cytotoxic Activities

Nickel (II) complex and heterogenized NiC@g-C₃N₄ complex showed an increase in lipid peroxidation and tissue damage as indicated by the increase in MDA levels in different examined organs (brain, liver, kidney and heart). It has been shown that Nickel fumes significantly upregulated reactive oxygen species and increased DNA damage. These alterations in MDA levels and lipids peroxidation are the cause for the cytotoxic activity and apoptosis of NIH/3T3 cells stimulated by nickel(II) derivatives [43]. MDA is the key completion product of lipid peroxidation [44]. Of note, the most affected organs are the brain and heart (Table 4). Moreover, NiC@g-C₃N₄ is more cytotoxic relative to NiC administered group.

To examine reactive oxygen species and antioxidants states of NiC and NiC@g-C₃N₄ complexes, we measured the oxidative stress biomarkers that includes GSH, SOD, GST, and MDA in response to nickel-administration for 14 consecutive days. The cellular oxidant/antioxidant defensive mechanism depends on the endogenous production of measured antioxidants. However, if ROS are caused at an wrong time or in too much amounts, or if antioxidant resistances are overwhelmed, negative effects of oxidative stress may arise. Apoptotic cell death was confirmed when the antioxidant defense system was significantly decreased by nickel administration. The tissue damage was highly reported for liver, brain and kidney in NiC@g-C₃N₄ administered rats compared with NiC group. In parallel, GSH and GST are mostly affected (P<0.05) in Liver and brain of NiC@g-C₃N₄ received rats when compared to NiC administered rats (Table 4).

Some published reports confirmed that NiSO₄ can reduce the GSH and SOD activities [45]. Another reporter suggests that NiNPs induced oxidative damage and stress, which decreased GSH and lipid peroxidation (LPO) in human lung epithelial A549 cells [46]. The NiCl₂ showed renal toxicity when administered orally and caused renal damage of rats through downregulation of mRNA expression levels

and antioxidant activities and enhanced free radicals generation, lipid peroxidation [47], and that are coincided with our findings. Same was reported in bursa fabricus of broilers [48] and rat testis [49].

It has been reported that sub-acute nickel exposure to rats resulted in impairment in behavior, neuronal microarchitecture alteration and oxidative stress in brain [50], liver [51] and heart [52]. In conclusion, in vivo experiments confirmed the cytotoxic impacts of newly synthesized nickel complexes (Table 4). They showed negative effect of antioxidants activities and increased lipids peroxidation and tissue damage for brain, liver, kidney and heart.

Table 4

Antioxidants system; MDA (nmol/ml); GSH (mg/g protein); GST (U/ g protein); GS-R (U/mL), and SOD (U/g protein) in different rat organs. *denotes significant relative to control groups. \$ denotes significant relative to NiC administered rats.

	Control	NiC	NiC@g-C ₃ N ₄
MDA			
Brain	6.21± 0.7	8.52±0.65*	9.23±0.18*
Liver	15.71±0.95	46.31±9.76*	72.42±16.4*\$
Kidney	70.31±14.54	100.42±26.9*	139.30±21.0*\$
Heart	65.31±14.3	78.3±11.4	89.19±15.6*
GSH			
Brain	28.31±5.21	30.51±3.2	42.29±7.60*\$
Liver	67.53±14.1	70.37±18.3	71.77±10.55
Kidney	70.51±16.1	67.41±19.1	71.44±18.10
Heart	65.41±12.22	64.21±17.5	66.08±15.30
GST			
Brain	25.31±2.8	28.81±1.9	24.99±2.58
Liver	17.81±1.54	20.72±2.11	46.21±2.86*\$
Kidney	1.31±0.08	1.27±0.04	1.64±0.15
Heart	10.31±1.04	15.43±3.2*	17.56±1.39*
GS-R			
Brain	0.91±0.06	0.84±0.04	1.55±0.30*
Liver	3.45±0.4	3.61±0.35	4.71±0.85
Kidney	4.31±0.76	5.54±1.08	5.49±1.07

Declarations

Declaration of Competing Interest

The authors declare that there are no conflicts of interest regarding the publication of this research paper.

Acknowledgements

References

1. V. Lobo, A. Patil, A. Phatak, N. Chandra, *Pharmacogn Rev.* **4**, 118 (2010)
2. A. Phaniendra, D.B. Jestadi, L. Periyasamy, *Indian J. Clin. Biochem.* **30**, 11 (2015)
3. F. Collin, *Int. J. Mol. Sci.* **20**, 2407 (2019)
4. F.I. Elshami, A.M. Ramadan, M.M. Ibrahim, I.M. El-mehasse, S. Al-Juaid, S.Y. Shaban, *Appl. Organomet. Chem.* **34**, 1 (2020)
5. A.M. Ramadan, S.Y. Shaban, M.M. Ibrahim, S.A. Sallam, F.I. El-Shamy, S. Al-Juaid, *J. Mat Sci.* **55**, 6457 (2020)
6. M.M. Ibrahim, S.Y. Shaban, A.M. Ramadan, M.A. Alruqi, G.A.M. Mersal, S.A. El-Shazly, S. Al-Juaid, *J. Mol. Struct.* **1198**, 126911 (2019)
7. M.M. Ibrahim, G.A.M. Mersal, S. Al-Juaid, S. El-Shazly, *J. Mol. Struct.* **166**, 1056 (2014)
8. S.Y. Shaban, A.M. Ramadan, M.M. Ibrahim, M.A. Mohamed, R. Van Eldik, *Dalton Trans.* **44**, 14110 (2015)
9. M.M. Ibrahim, A.M. Ramadan, M.A. Mohamed, S. Imam, M. Soliman, *J. Coord. Chem.* **68**, 4296 (2015)
10. M.A. Ramadan, M.M. Ibrahim, I.M. El-Mehasseb, *J. Coord. Chem.* **65**, 2256 (2012)
11. Y. Wang, N. Zhang, R. Hübner, D. Tan, M. Löffler, S. Facsko, E. Zhang, Y. Ge, Z. Qi, C. Wu, *Adv. Mater. Interfaces* **6**, 1801664 (2019)
12. B. Coulson, M. Isaacs, L. Lari, R.E. Douthwaite, A. Duhme-Klair, *Chem. Commun.*, 7450 (2019)
13. Y. Kumar, S. Rani, J. Shabir, L.S. Kuma, *ACS Omega* **5**, 1325 (2020)
14. W. Zhen, X. Yuan, X. Ning, X. Gong, C. Xue, *ACS Appl. Mater. Interfaces* **12**, 868 (2019)
15. Y. Xu, C. Du, C. Zhou, S. Yang, *Chem. Commun.* **56**, 7171 (2020)
16. A. Kumar, P. Kumar, C. Joshi, S. Ponnad, A.K. Pathak, A. Ali, B. Sreedhard, S.L. Jain, *Green Chem.* **18**, 2514 (2016)
17. M.J. Lima, A.M.T. Silva, C.G. Silva, J.L. Faria, J.L. Faria, *J. Catal.* **353**, 44 (2017)
18. I.A. Abdelhafeez, X. Zhou, Q. Yao, Z. Yu, Y. Gong, J. Chen, *ACS Omega* **5**, 4181 (2020)
19. A.M. Ramadan, S.Y. Shaban, M.M. Ibrahim, A.A.-H. Abdel-Rahman, S.A. Sallam, S.A. Al-Harbie, W. Omara, *New J. Chem.* **44**, 6331 (2020)
20. K. Maeda, D. An, R. Kuriki, D. Lu, O. Ishitani, B. J. *Org. Chem.* **14**, 1806 (2018)
21. SAINT, V6.02, A.X.S. Bruker, Madison, WI (1999)
22. G.M. Sheldrick, SADABS, Area-Detector Absorption Correction, Göttingen, Germany (1996)
23. G.M. Sheldrick, S.H.E.L.X.S. Program, Program for Crystal Structure Determination, Göttingen, Germany (1997)

24. N.N. Ghosh, 1984. Fundamentals of Experimental Pharmacology. 2nd Edn., Scientific Book Agency, Kolkatta, ISBN: 81-902965-0-7, pp: 175-176
25. S. Reitman, S. Frankel, J. Clin. Pathol. **28**, 56 (1957)
26. H.U. Bergmeyer, H.U., 1974. Methods of Enzymatic Analysis. 2nd Edn., Academic Press, New York, ISBN: 0895732424, pp: 534
27. W.H. Habig, M.J. Pabst, W. B. Jakoby. J. of Biol. Chem. **249**, 7130 (1974) 713.
28. P. Kakkar, B. Das, P.N. Visvanathan, Industrial Journal of Biochemistry and Biophysics **197**, 588 (1972)
29. G.L. Ellaman, G. L. Arch. Biochem. Biophys. **82**, 70 (1959)
30. S.K. Jain, R. McVie, J. Duett, J.J. Herbst, Diabetes **38**, 1539 (1989)
31. P.N. Brady, M.A. Macnaughtan, Anal. Biochem. **491**, 43 (2015)
32. F. Yilmaz, V.T. Yilmaz, E. Bicer, O. Büyükgüngör, Z. Naturforsch. B, **61b**, 275 (2006)
33. M.M. Ibrahim, A.M. Ramadan, M.A. Mohamed, S. Imam, M. Soliman, J. Coord. Chem. **68**, 4296 (2015)
34. M.M. K.A.Fraser, Harding, J.Chem. Soc., Dalton Trans. 415 (1967)
35. T. Sakurai, H. Iwasaki, T. Katano, Y. Nakahashi, Acta Crystallogr. Sect. B **34**, 660 (1978)
36. M.M. Morelock, M.L. Good, L.M. Trefonas, D. Karraker, L. Maleki, H.R. Eichelkerger, R. Magesti, J. Dodge, J. Am. Chem. Soc. **101**, 4858 (1979)
37. V.T. Yilmaz, C. Icel, F. Suyunova, M. Aygun, B. Cevatemrec, E. Ulukayad, New J. Chem. **41**, 8092 (2017)
38. V.W. Yam, A.K. Chan, E.Y. Hong, Nat. Rev. Chem. **4**, 528 (2020) 528
39. A. Kumar, P. Kumar, C. Joshi, S. Chetan, A.K. Ponnada, A. Pathak, B. Ali, S.L. Sreedhar, Jain, Green Chem. **18**, 2514 (2016)
40. M. Sadhukhan, S. Barman, J. Mater. Chem. A **1**, 2752 (2013)
41. B.Y. Zhao, Z. Liu, W. Chu, L. Song, Z. Zhang, D. Yu, Y. Tian, S. Xie, L. Sun, Adv. Mater. **20**, 1777 (2008)
42. (a) L. Ge, Mater. Lett., **65**, 2652 (2011); (b) M. Groenewolt and M. Antonietti Adv. Mater., 2005, 17, 1789–1792
43. Y. Wang, S. Wang, L. Jia, L. Zhang, J. Ba, D. Han, C. Yu, Y. Wu, Int J. Environ Res. Public Health. **13**, 629 (2016)
44. J. Sun, W. Guo, Y. Ben, J. Jiang, C. Tan, Z. Xu, X. Wang, C. Bai. Crit. Care Med. **36**, 1205 (2008)
45. G.H. Zhen, C.M. Liu, J.M. Sun, Z.J. Feng, C. Cheng, Toxicol. **147**, 105 (2014)
46. M. Ahamed, Toxicol. In Vitro **25**, 930 (2011)
47. H. Guo, B. Wu, H. Cui, X. Peng, J. Fang, Z. Zuo, J. Deng, X. Wang, J. Deng, S. Yin, J. Li, K. Tang, Biol. Trace Elem. Res. **162**, 288 (2014)
48. S. Yin, H. Guo, H. Cui, X. Peng, J. Fang, Z. Zuo, J. Deng, X. Wang, K. Tang, J. Li, Biol. Trace Elem. Res. **171**, 214 (2016)
49. L. Kong, W. Hu, C. Lu, K. Cheng, M. Tang, Chemosphere. **218**, 259 (2019)

50. O.M. Ijomone, S.O. Okori, O.K. Ijomone, A.P. Ebokaiwe, Drug Chem. Toxicol. **41**, 377 (2018)
51. S. Yu, F. Liu, C. Wang, J. Zhang, A. Zhu, L. Zou, A. Han, J. Li, X. Chang, Y. Sun, Mol. Med. Rep. **17**, 3133 (2018)
52. R.C. Reddy, B. Devaranavadi, S.M. Yendigeri, S. Bagali, R.V. Kulkarni, K.K. Das, Biol. Trace Elem. Res. **195**, 178 (2020)

Scheme

Scheme 1 is available in the Supplementary Files section.

Figures

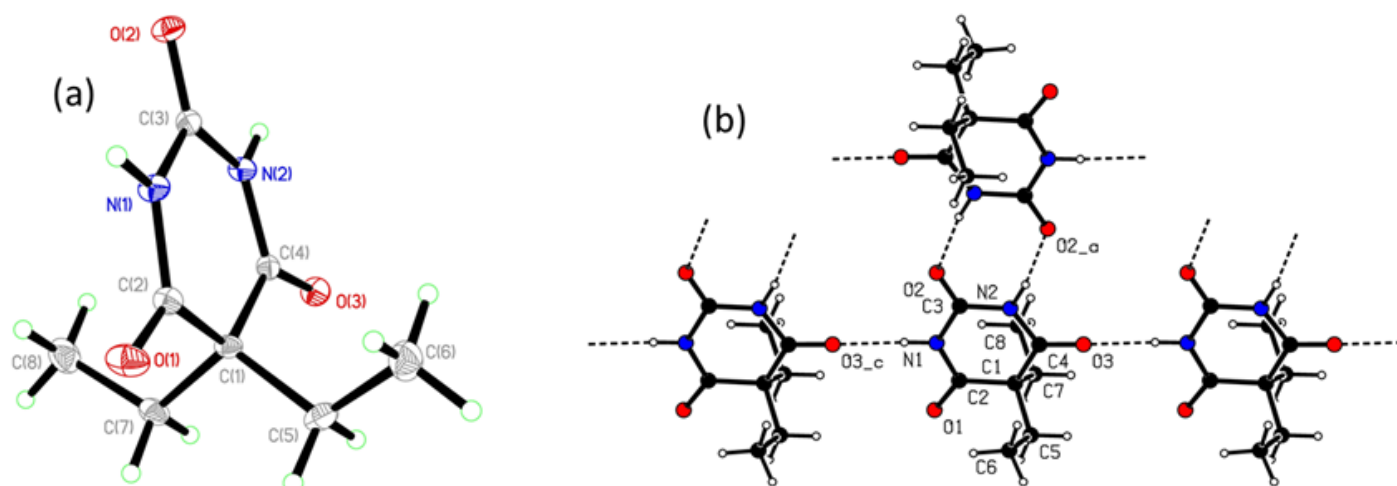


Figure 1

Molecular structure of Barb-H (a) ORTEP drawing with thermal ellipsoids of 50% probability level; (b) Projection along *c* axis, showing the geometry in the ribbons which are formed from the ligand Barb-H. Inter H-bonding presented.

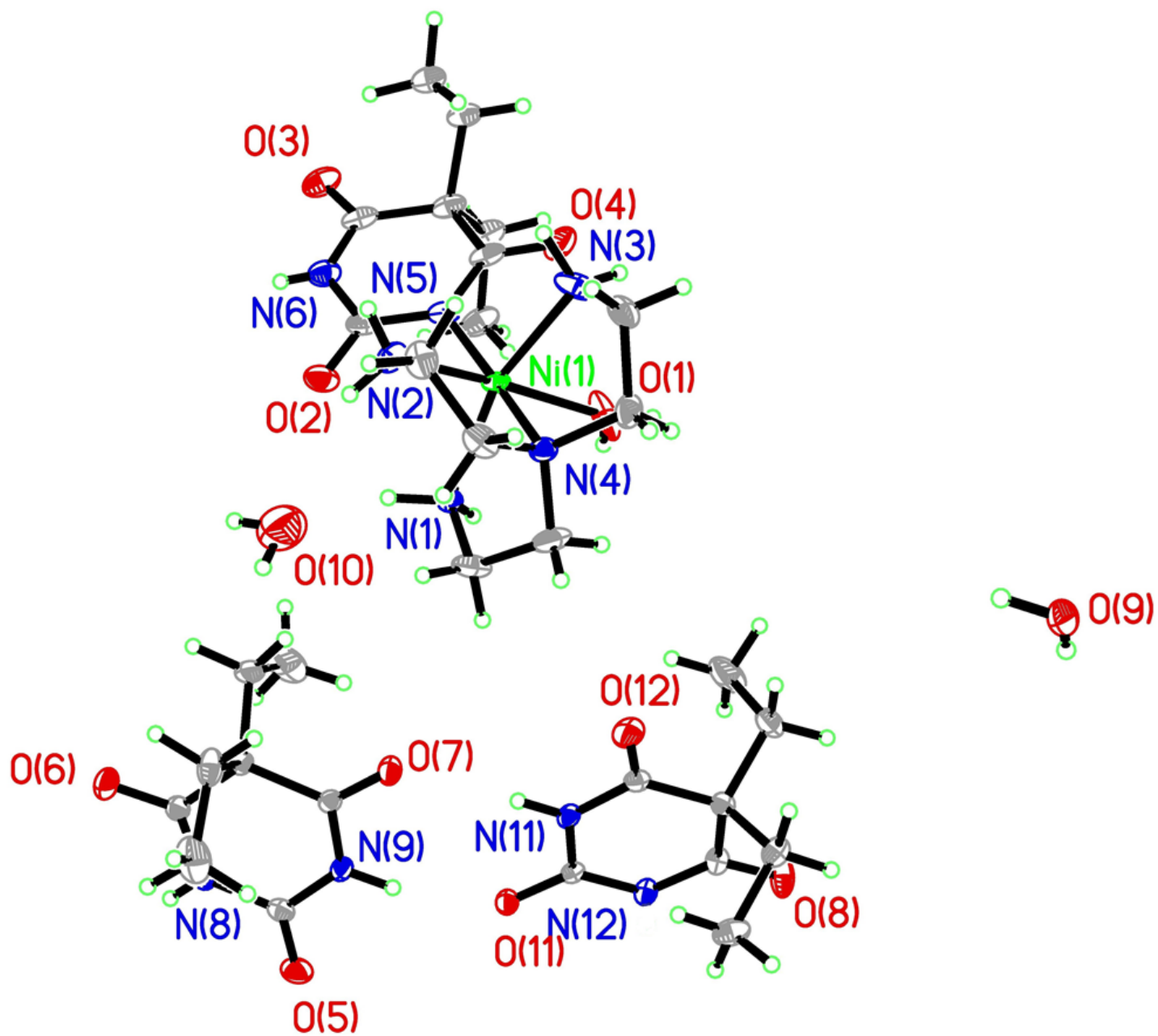


Figure 2

ORTEP drawing of nickel(II) complex NiC with thermal ellipsoids of 50% probability level.

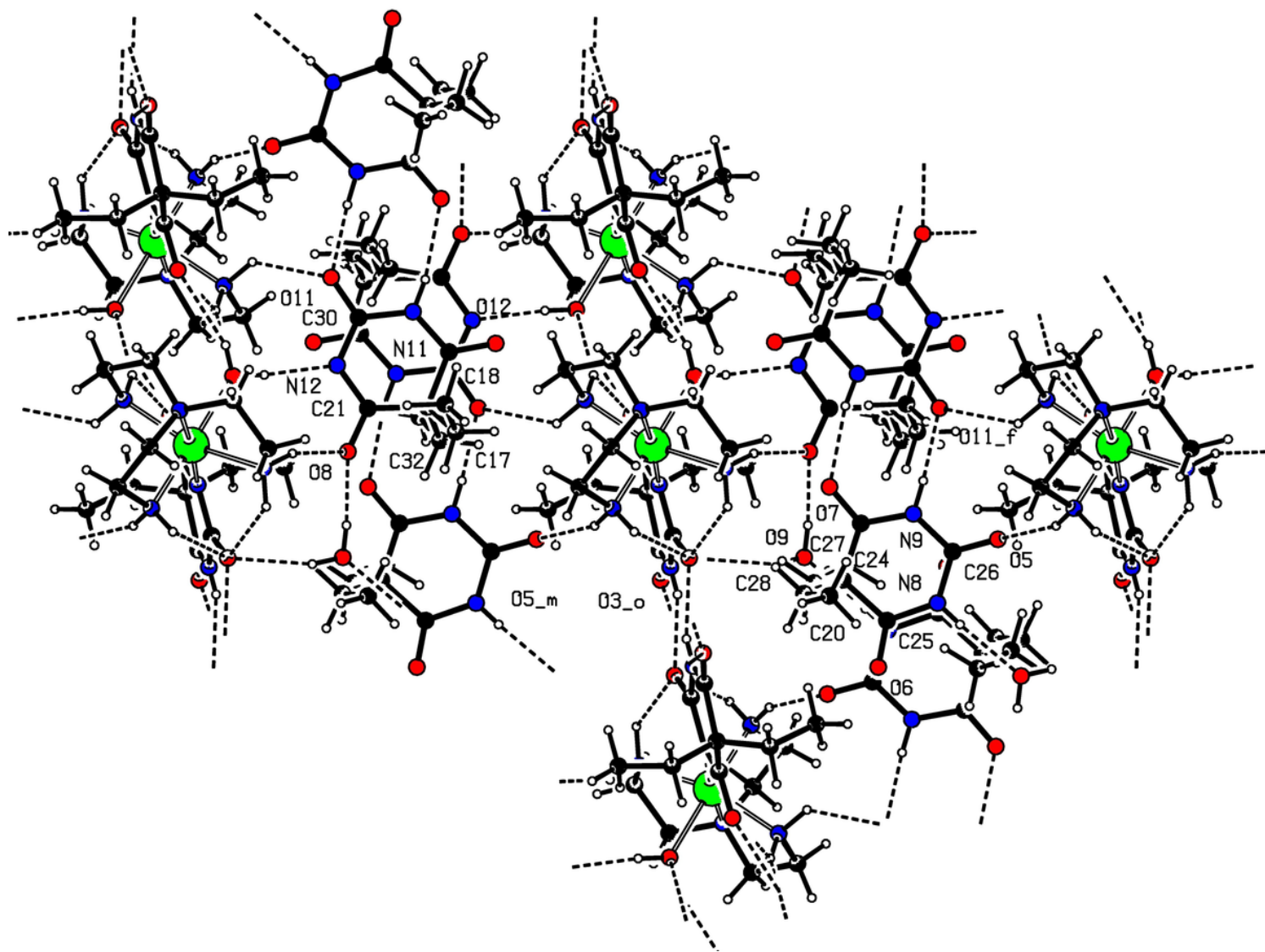


Figure 3

Projection along *c* axis of nickel(II) complex **NiC**, describing the geometry in the ribbons which are formed from the dimer NiC. Inter and intra H-bonding presented.

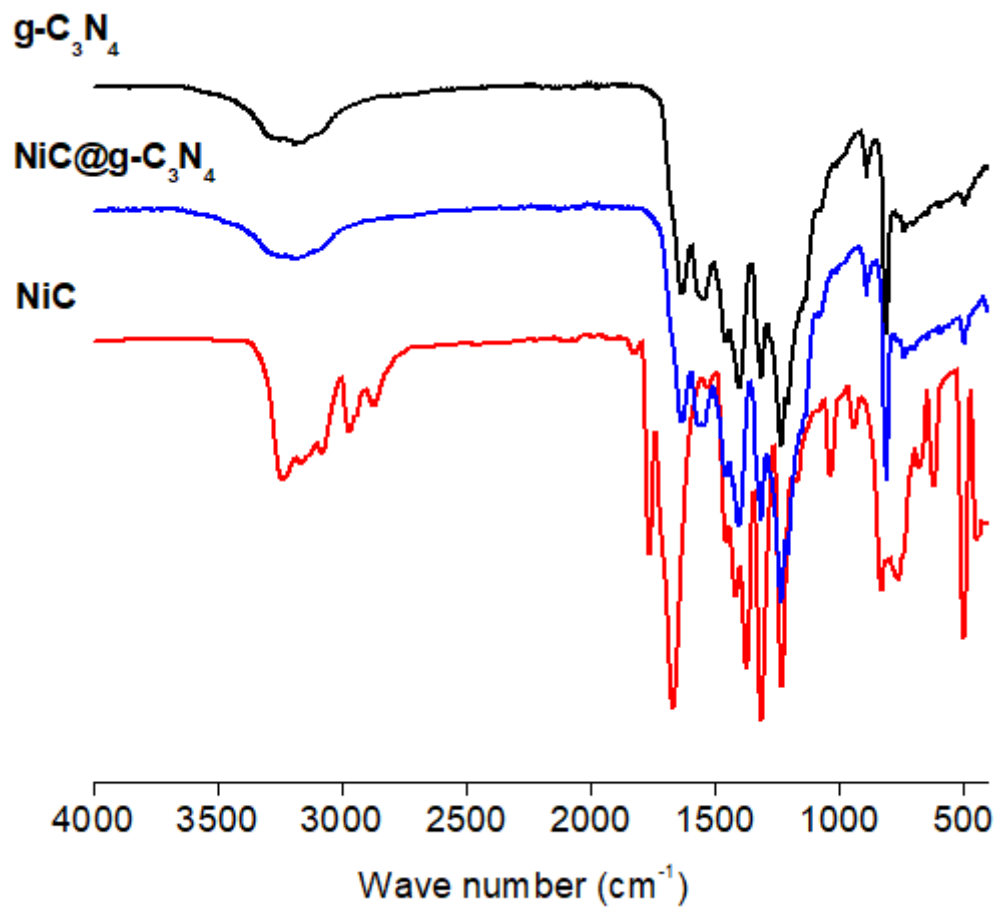


Figure 4

FT-IR of the nickel(II) complex NiC , $\text{g-C}_3\text{N}_4$ nanosheets, and the hybrid composite $\text{NiC@g-C}_3\text{N}_4$

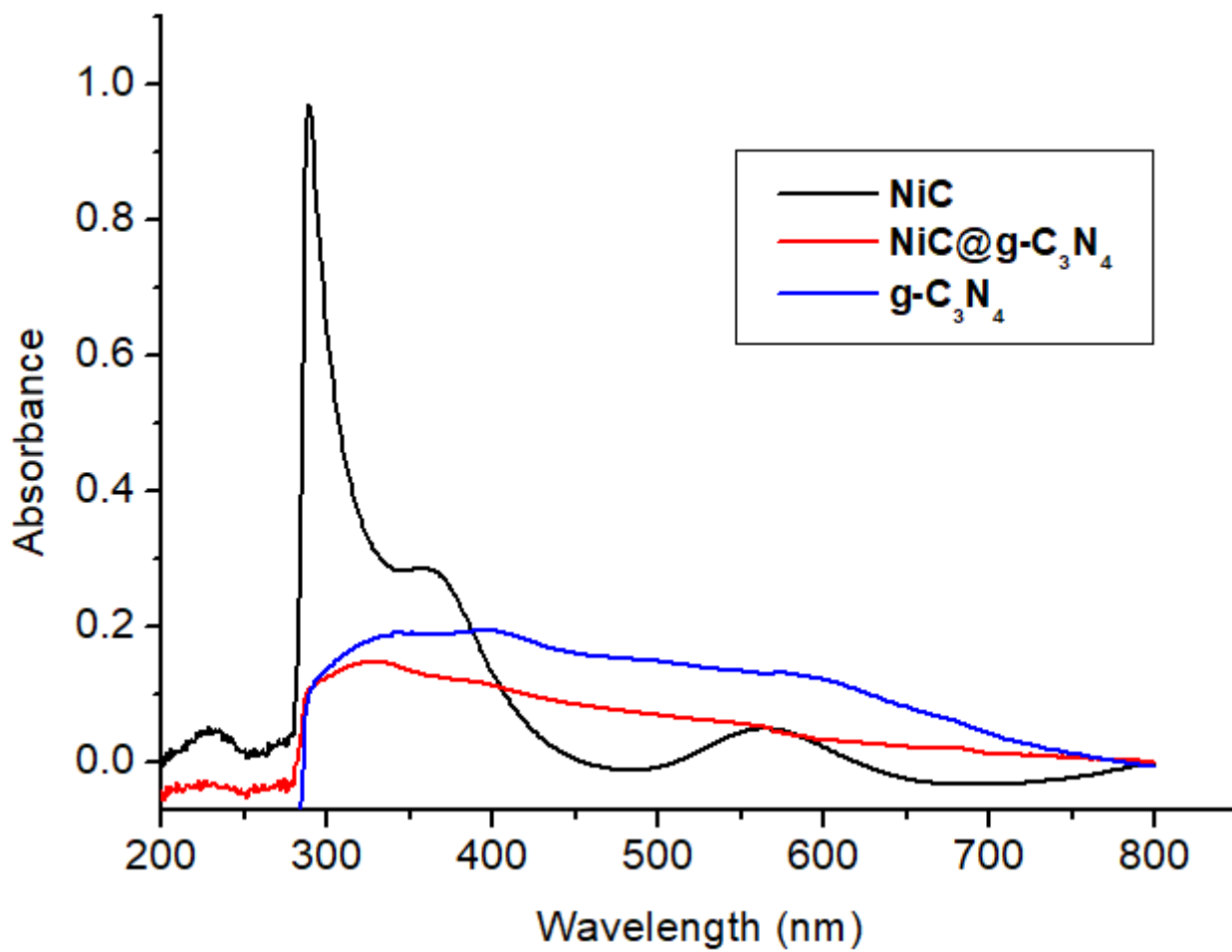


Figure 5

UV-Vis absorption spectra of: a) NiC; b) g-C₃N₄, and c) NiC@g-C₃N₄

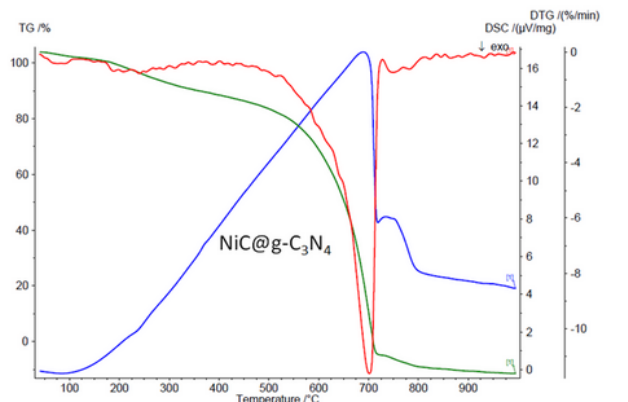
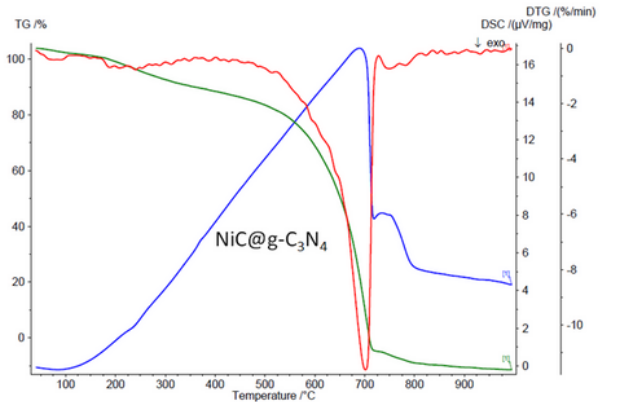
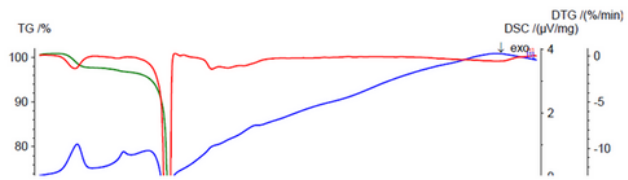
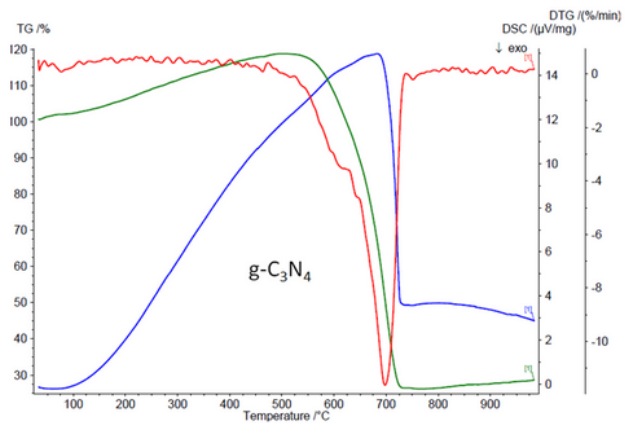


Figure 6

TGA-DSC thermograms of $g\text{-C}_3\text{N}_4$ nanosheets, complex NiC, and NiC@ $g\text{-C}_3\text{N}_4$ composite.

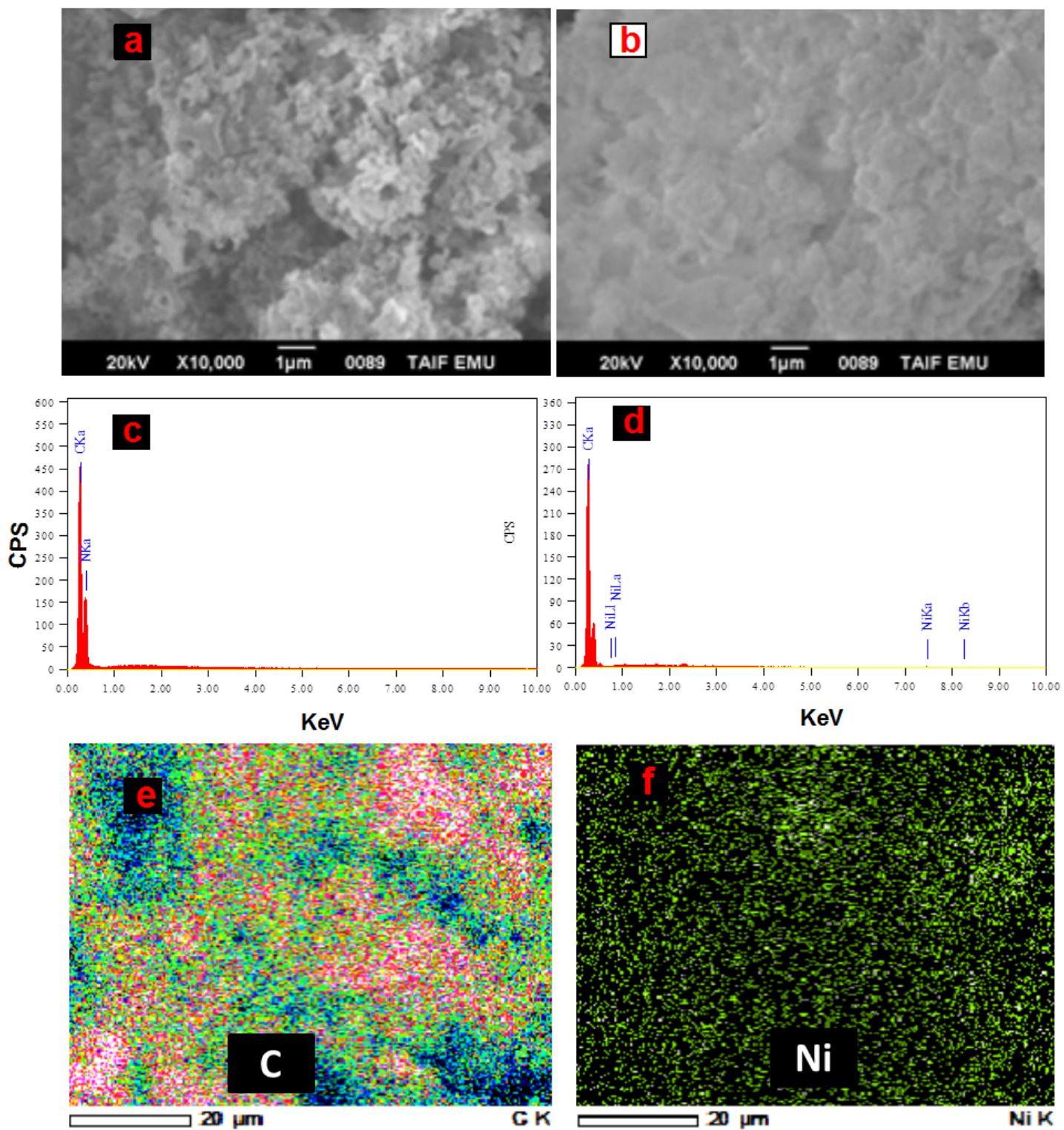


Figure 7

SEM images of (a) g-C₃N₄, (b) NiC@g-C₃N₄; EDX pattern of (c) g-C₃N₄; (d) NiC@g-C₃N₄ and elemental mapping for (e) C; (f) Fe.

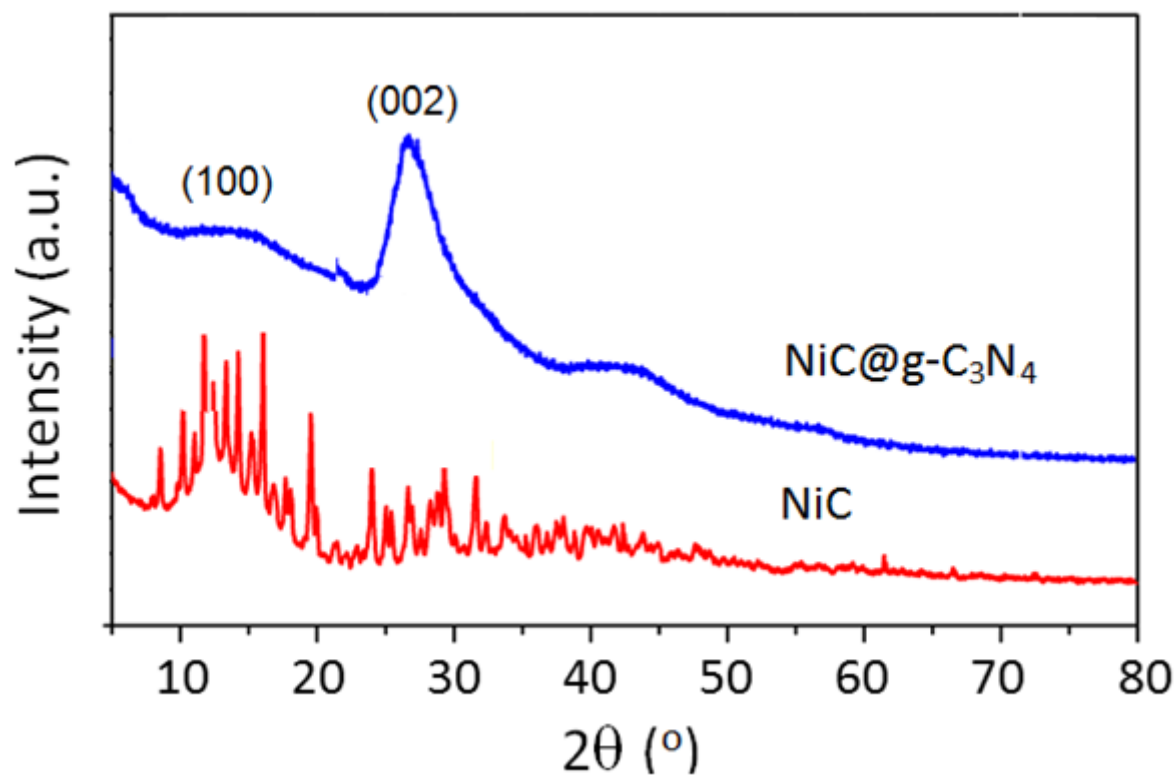


Figure 8

XRD patterns of **NiC**, and **NiC@g-C₃N₄**

Supplementary Files

This is a list of supplementary files associated with this preprint. Click to download.

- [Scheme1.png](#)